International Journal of Extreme Manufacturing

Abnormal interfacial bonding mechanisms of multi-material additive-manufactured tungsten–stainless steel sandwich structure

To cite this article: Chao Wei *et al* 2022 *Int. J. Extrem. Manuf.* **4** 025002

OPEN ACCESS
IOP Publishing | IMMT
International Journal of Extreme Manufacturing
Int. J. Extrem. Manuf. 4 (2022) 025002 (16pp)
https://doi.org/10.1088/2631-7990/ac5f10

Abnormal interfacial bonding mechanisms of multi-material additive-manufactured tungsten–stainless steel sandwich structure

Chao Wei[1], Heng Gu[2], Yuchen Gu[3], Luchao Liu[3], Yihe Huang[1], Dongxu Cheng[1], Zhaoqing Li[1] and Lin Li[1,*]

[1] Laser Processing Research Centre, Department of Mechanical, Aerospace and Civil Engineering, The University of Manchester, Manchester M13 9PL, United Kingdom
[2] School of Mechanical Engineering, Jiangsu University, Zhenjiang, People's Republic of China
[3] College of Engineering, Swansea University, Swansea SA1 8EN, United Kingdom

E-mail: lin.li@manchester.ac.uk

Received 26 November 2021, revised 4 January 2022
Accepted for publication 18 March 2022
Published 12 April 2022

Abstract

Tungsten (W) and stainless steel (SS) are well known for the high melting point and good corrosion resistance respectively. Bimetallic W–SS structures would offer potential applications in extreme environments. In this study, a SS→W→SS sandwich structure is fabricated via a special laser powder bed fusion (LPBF) method based on an ultrasonic-assisted powder deposition mechanism. Material characterization of the SS→W interface and W→SS interface was conducted, including microstructure, element distribution, phase distribution, and nano-hardness. A coupled modelling method, combining computational fluid dynamics modelling with discrete element method, simulated the melt pool dynamics and solidification at the material interfaces. The study shows that the interface bonding of SS→W (SS printed on W) is the combined effect of solid-state diffusion with different elemental diffusion rates and grain boundary diffusion. The keyhole mode of the melt pool at the W→SS (W printed on SS) interface makes the pre-printed SS layers repeatedly remelted, causing the liquid W to flow into the sub-surface of the pre-printed SS through the keyhole cavities realizing the bonding of the W→SS interface. The above interfacial bonding behaviours are significantly different from the previously reported bonding mechanism based on the melt pool convection during multiple material LPBF. The abnormal material interfacial bonding behaviours are reported for the first time.

Keywords: multi-material additive manufacturing, laser powder bed fusion, interfacial bonding, element diffusion, keyhole mode

* Author to whom any correspondence should be addressed.

2631-7990/22/025002+16$33.00

1. Introduction

The melting temperature of tungsten (W) is higher than that of any other metal on the earth. It is also featured by its excellent sputtering resistance, plasma radiation resistance and low thermal expansion coefficient [1]. Therefore, many plasma-facing components (e.g. first walls) of nuclear fusion reactors are made of W, in order to hold the strength at extremely high temperatures and shield energetic α- and γ-radiations [2]. However, high brittleness is a disadvantage of W. In the nuclear reactor's high temperature and high radiation environment, the surface of W can be eroded by high-energy rays quickly and generates dust, which affects the plasma parameters [3].

Combining W with other metals such as nickel (Ni) and iron (Fe) can reduce the brittleness of W and increase its ductility. There are two routes to combine W with other metals. The first is to sinter W powder with other relatively low melting point metallic powders through powder metallurgy [4] and powder injection moulding [5] to produce tungsten heavy alloys (WHAs). Recently, researchers have also studied the fabrication of WHAs by three-dimensional (3D) printing technologies, including laser-based powder bed fusion (LPBF) [6] and bound metal deposition [7]. However, there has been no previous studies on additive manufacturing (AM) of W–stainless steel (SS) bimetallic structure, which requires special equipment, not widely available. The second route is to join W plates/blocks with other metals via diffusion bonding (DB) [8] or hot isostatic pressing (HIP) [9]. DB and HIP cannot manufacture parts with complex 3D geometry, so it is not feasible to fabricate complex W-involved multi-material components via these traditional methods.

The production of 3D components composed of dissimilar materials through AM methods is an emerging field, which is promising to overcome the above drawbacks of traditional processes. The latest development of multi-material LPBF technology with multi-material powder deposition functions provides an opportunity to manufacture W–SS bimetallic structures. An ultrasonic-assisted multi-material LPBF technology was developed by the team from The University of Manchester [10]. Chadha [11] investigated an iron–cobalt alloy system fabricated via LPBF. Goh *et al* [12] reported the recent progress of AM of multi-layered and multi-material electronics. Chao *et al* [13, 14] reviewed recent progress of multi-material LPBF mechanism and material characteristics. However, until now, there has been no reported work on AM-fabricated multi-material components involving W and SS, although studies on AM-production of W heavy alloys have been reported [6, 7] and a W block printed on a dissimilar material substrate [15].

W and SS present completely different physical properties, e.g. melting temperature, material density and thermal conductivity. These differences may pose a challenge to the manufacture of W–SS bimetal structures. So far, there has been no previous studies reported on how these differences affect the W–SS interfacial bonding during AM.

In this study, we investigated the feasibility of LPBF printing a sandwich structure comprised of 316L SS and W, focusing on the characteristics of the material interfaces of the sandwich structure. Modelling and simulation tool revealed the effect of deposition sequences on the molten pool's temperature gradient and its thermodynamic behaviour. The study reveals the effect of melting point differences on the interfacial bonding mechanisms of dissimilar materials in multi-material LPBF. The high-temperature liquid phase W causes the pre-printed SS layer to enter a keyhole mode, which is the fundamental reason for the W–SS interface bonding. In the case that the pre-printed W layer is not remelted, the mutual diffusion of dissimilar metallic elements at the interface can also make SS bond to the solid W layers.

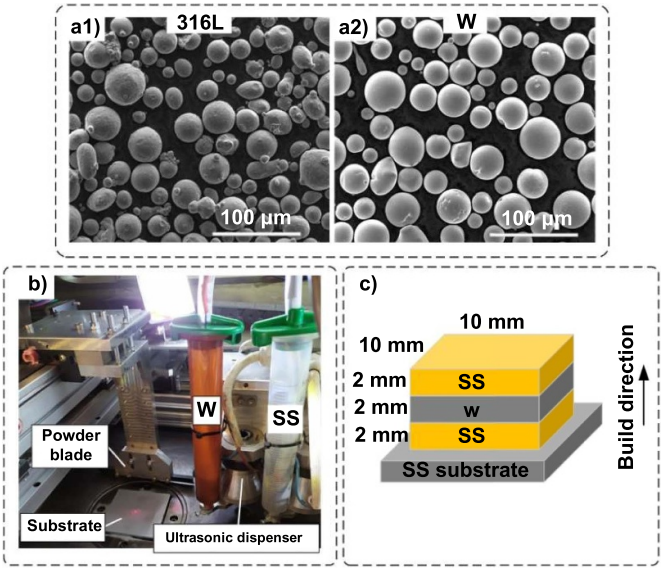

Figure 1. Micrographs of (a1) 316L SS powder and (a2) pure W powder used in this study; (b) the home-made multiple material ultrasonic powder dispensing system used in this study; (c) schematic of the LPBF-printed SS–W–SS sandwich structure.

2. Experimental materials and procedure

2.1. Materials

As shown in figure 1(a1), the spherical 316L SS powder, supplied by LPW Ltd, had a particle size distribution arranging from 10 to 45 μm. The spherical W powder (particle size: 15–45 μm, as shown in figure 1(a2)) was provided by TEKNA advanced materials Inc., Canada. Samples were printed on sand-blasted 316L plates in this study.

2.2. Experimental setup

Our previous publication [16] described our home-made LPBF system in detail. Compared with commercial LPBF machines, this homemade system utilized an ultrasonic-driven powder dispensing device (figure 1(b)) to deposit different powders at desired locations on the powder bed. W and 316L powders were stored in independent cylinders with fine powder feeding nozzles (inner diameter of nozzle: 450 μm for 316L and 300 μm for W, respectively), and were

Table 1. Laser processing parameters of this study.

Position		Laser thickness (t, mm)	Laser power (P, kW)	Hatch distance (h, mm)	Scanning speed (v, m s^{-1})	$E_d = \frac{P}{v \cdot h \cdot \leqslant t}$ (J mm^{-3})	References
SS	The 1st–67th layers	0.03	0.2	0.07	1.2	79.4	[23]
W	The 68th–135th layers	0.03	0.4	0.1	0.725	183.9	[17]
SS	The 136th–203th layers	0.03	0.2	0.07	1.2	79.4	[23]

spread on demand through vibration activated with the ultrasonic transducers; the powder dispensers moved along the computer-controlled Cartesian x–y motion system to deposit pre-designed patterns comprised of different powders on the powder bed. A soft blade driven by a linear stage was used to compact, level and smooth the powder deposited by the ultrasonic dispensers.

2.3. Experimental procedure

As illustrated in figure 1(c), a sandwich structure comprised of three parts was printed in the order SS, W, SS.

The focus of this research was on the influence of the differences in physical properties of W–SS on their interfacial bonding behaviors. LPBF of pure W [17–19] and LPBF of pure 316L [20–23] have been extensively studied previously. Even if the processed materials were the same, the laser processing parameters reported in these studies, especially the laser energy density, often varied greatly, which might be caused by equipment differences. Our preliminary experiments found that the LPBF processing parameters of W reported in the article [17] and that of 316L reported in the article [23] were suitable on the special LPBF equipment used in the present study. Therefore, these two sets of parameters were used to produce the W and 316L parts in this study, as shown in table 1. The laser volume energy density (E_d) in table 1 was calculated based on the formula given by Caiazzo *et al* [24].

2.4. Material characterization

The LPBF-printed sandwich structure was cross-sectioned to 1.5 mm slabs with a precision disk cutting machine. The thin slabs were hot mounted in black conductive polymer and then ground and polished. The polished specimens were chemically etched. Kroll's Reagent (water 91%–97%, hydrofluoric acid 1%–3%, nitric acid 2%–6%) and the etchant (potassium hydroxide 10 g, potassium hexacyanoferrate (III) 10 g, water 200 ml) were used to respectively etch the 316L part and the W part.

All optical micrographs in this study were obtained using a digital optical microscope (VHX-5000, KEYENCE) equipped with a differential interference contrast module with a universal objective lens (VH-Z100UR, KEYENCE). The element distribution patterns at the dissimilar material interfaces were characterized using a scanning electron microscope–energy-dispersive x-ray spectroscopy (SEM–EDS) system (Sigma VP FEG SEM, Zeiss). The phases of the base materials and the two interfaces were examined with a high-resolution x-ray diffractometer (XRD, Smartlab, Rigaku). Electron backscatter diffraction (EBSD) patterns of the material interfaces were acquired using an EBSD system (JSM 7800F, JEOL). A nano hardness tester (Ti950, Hysitron) measured the hardness of different regions on the specimen. Nano-hardness measurements were repeated ten times to determine the mean value.

3. Numerical modelling

Molten pool dynamics at the two materials' interfaces were simulated based on computational fluid dynamics–discrete element method (CFD–DEM) integrated modelling framework developed in our previous investigation [25, 26].

Two DEM models were set up in this modelling work, including the 30 μm thick SS powder layer on the 120 μm thick solid W substrate (i.e. the SS→W interface) and the 30 μm thick W powder layer on the 120 μm thick solid SS substrate (i.e. the W→SS interface). Figures 2(a) and (b) illustrate their initial morphologies. The process parameters employed in these two simulations were the same as those used in physical experiments (see table 1).

The thermal properties of 316L SS and W used in the CFD simulation are presented in table 2.

4. Experimental results

4.1. Macro- and micro-structures of the LPBF-printed SS–W–SS sandwich structure

As shown in figure 3(a), no visible delamination and cracks were observed on the LPBF-printed SS–W–SS sandwich sample.

4.1.1. Microstructure of the base materials. The microstructures of SS at the top and SS at the bottom were both organized by overlapping and continuous melt pool tracks (a 'fish-scale' pattern, see figures 3(b1) and (b3)), and the typical grain structure was cellular-columnar grains oriented along the build direction of LPBF. These cellular-columnar grains grew across several build layers, a typical LPBF-fabricated SS microstructure [29, 30]. Rapid cooling and solidification of the melt pools generate the most significant temperature gradient along the build direction, leading to the fastest growth velocity of crystal grains [31].

The microstructure of the W region in the sample was comprised of columnar grains (figure 3(b2)), similar to the LPBF-printed W microstructure described in the previous investigation [32].

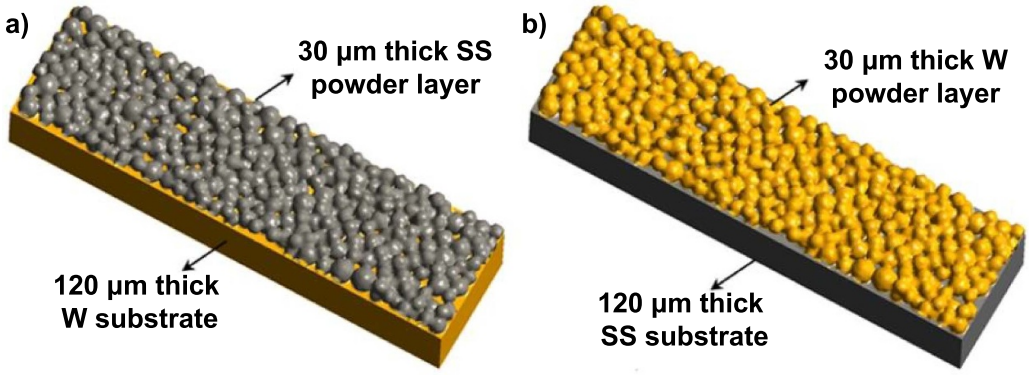

Figure 2. The initial DEM model morphologies of (a) the SS powder layer deposited on the solid W substrate and (b) the W powder layer deposited on the solid SS substrate.

Table 2. Thermal properties of 316L SS [27] and W [28].

Symbol	Nomenclature	316L	Tungsten
T_s	Solidus temperature (K)	1658	3695
T_l	Liquidus temperature (K)	1723	3695
ρ_s	Solidus density (kg m^{-3})	$8084 - 0.4209T - 3.894 \times 10^{-5}T^2$	$19\,250 - 0.266207 \times (T - 293.15) - 3.0595 \times 10^{-6} \times (T - 293.15)^2 - 9.5185 \times 10^{-9} \times (T - 293.15)^3$
ρ_l	Liquidus density (kg m^{-3})	$7433 - 0.0393T - 1.8 \times 10^{-4}T^2$	$16\,267 - 0.7679 \times (T - 3695) - 8.091 \times 10^{-5} \times (T - 3695)^2$
k_s	Solidus thermal conductivity (W m^{-1} K^{-1})	$9.248 + 0.01571T$	$149.441 - 45.466 \times 10^{-3}T + 13.193 \times 10^{-6}T^2 - 1.484 \times 10^{-9}T^3 + 3.866 \times 10^{6}/T^2$
k_l	Liquidus thermal conductivity (W m^{-1} K^{-1})	$12.41 + 0.003279T$	$66.6212 + 0.02086 \times (T - 3695) - 3.7585 \times 10^{-6} \times (T–3695)^2$
μ	Viscosity (kg m^{-1} s^{-1})	$10^{(2358.2/T\ -\ 3.5958)}$	$0.16 \times 10^{-3}e^{(14\,674/T)}$
σ	Surface tension (kg s^{-2})	1.6	2.48
$d\sigma/dt$	Surface tension coefficient (kg s^{-2} K^{-1})	-0.8×10^{-3}	-0.31×10^{-3}
L_m	Latent heat (J kg^{-1})	2.7×10^5	2.84×10^5
C_p	Heat capacity (J kg^{-1} K^{-1})	775	132

4.1.2. Macro- and micro-structures of the material interfaces.

4.1.2.1. SS→SS interface. The interface between the SS part at the sample's bottom and the SS substrate presented a typical metallurgical bonding microstructure. Neat fish-scale solidification lines appeared at the top of the substrate (see figure 3(b4)). This phenomenon indicated that the laser beam completely penetrated the powder layer and melted the powder particles around the laser beam spot to form a melt pool. Meanwhile, part of the laser energy and the heat transfer from the heat conduction of the liquid metal also remelted the surface of the substrate, enhancing the wettability between the liquid-phase material and the solid-phase base [33], avoiding the balling phenomenon. It also enhanced the mutual diffusion of elements in the powder material and the substrate material because of Marangoni convection in the melt pool [34]. It achieved good metallurgical bonding to the substrate.

4.1.2.2. SS→W interface. The SS→W (SS printed on W) interface (figure 3(b5)) was completely different from the above-mentioned SS→SS interface and did not show the solidification lines of melt pools; the pre-printed W layers still maintained their original morphology. The W particles (labelled by arrows in figure 3(b5), may have been adhered on and carried by the powder blade) remaining on the top of W layers were not able to be fused by the low energy density for SS. It may be due to the big melting temperature difference between W and SS (3695 and 1658 K respectively). No cracks, pores, and delamination defects were found at this interface, evidenced by the magnified SEM image (figure 3(c1)). The unmelted W particles were completely embedded in the molten SS layers, and no pores or cracks were found around them.

All the above phenomena indicated that liquid SS presented acceptable hydrophilicity on the solid W, so liquid SS could be firmly attached to the surface of W. However, it could not explain that, after high-frequency heating–cooling thermal circles during LPBF, why the newly-printed SS layers still firmly adhered to the pre-printed solid-state W substrate without warping and delamination. The EDS result and the EBSD result will provide further insights into the causes.

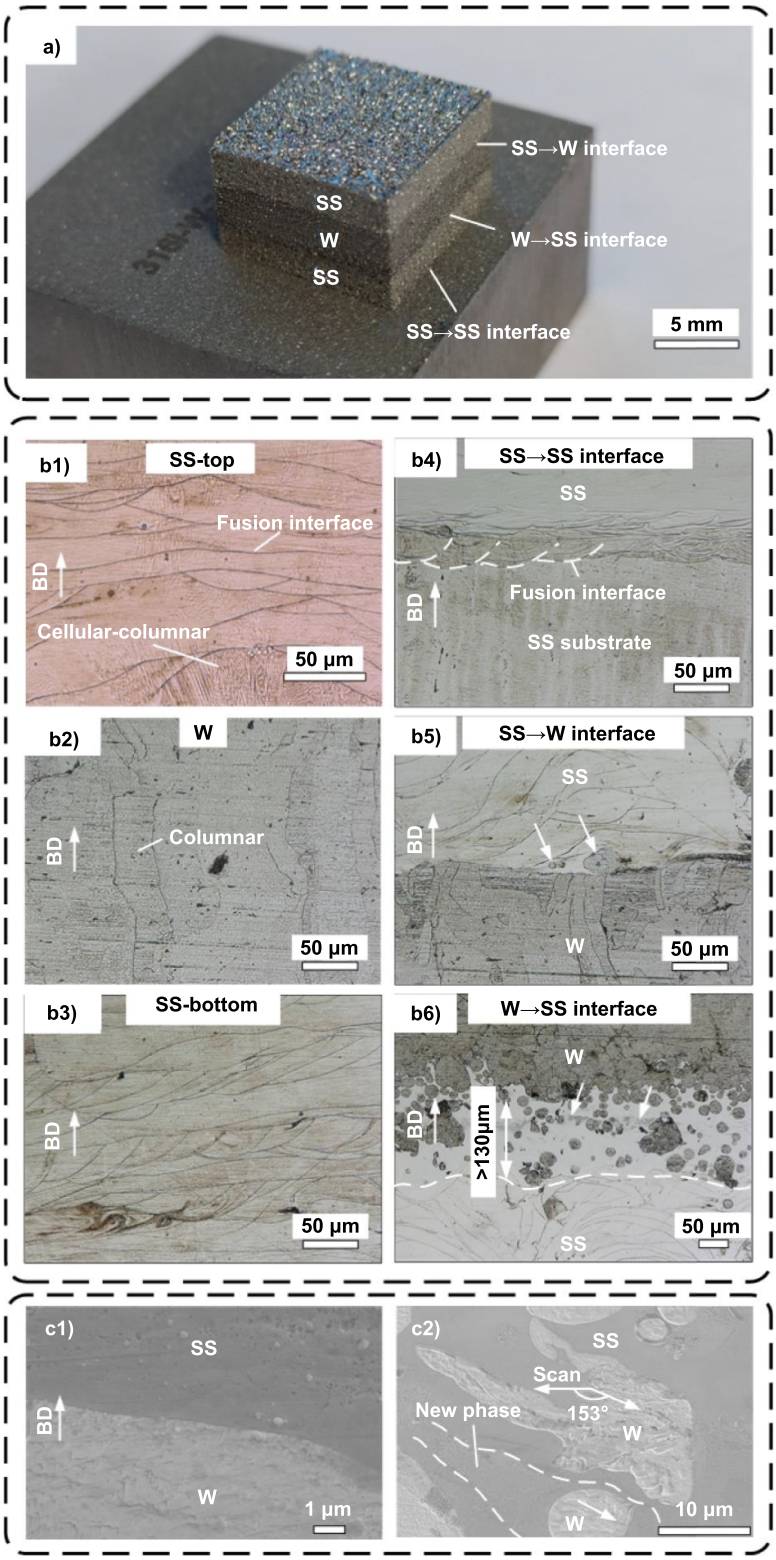

Figure 3. (a) An LPBF-printed SS–W–SS sandwich sample; (b1)–(b3) the microstructures of cross-sections at SS (top), W, and SS (bottom) parts; (b4)–(b6) the microstructures of the cross-sections at different material interfaces; (c1), (c2) the magnified SEM graphs of the cross-sections at different interfaces.

4.1.2.3. W→SS interface. The W→SS (W printed on SS) interface (figure 3(b6)) showed a totally different morphology compared with the SS→W interface (figure 3(b5)). The high laser energy density for melting W (183.91 J mm^{-3}) resulted in the remelting zone of the pre-printed SS layers as deep as 130 μm. In the remelting zone, a large number of small particles with approximately spherical shapes and large particles with irregular shapes appeared, and a mixed zone of

elements (labelled with arrows in figure 3(b6)) appeared as well.

The keyhole mode of LPBF described by Chen *et al* [35] could be employed to explain the above phenomenon. Excessive laser energy density caused the melt pool at the W→SS interface to enter a keyhole mode. In this mode, the high temperature vaporized the material to create a cavity (i.e. keyhole) in the pre-printed SS layers, and then the laser beam directly shot into the cavity, and multiple refractions occurred in it. It allowed more laser energy to be absorbed by the SS layers, further increasing the melt pool depth and width. The cavity collapsed later, and the liquid W flew into the keyhole. Because of the Marangoni convection, liquid W mixed with the elements of SS and may produce a new phase. The thermal conductivity of W is greater than that of SS (174 W m^{-1} K^{-1} and 14.0–15.9 W m^{-1} K^{-1} respectively). According to Newton's law of cooling, materials with high thermal conductivity cool faster [36]. Hence, W in the melt pool solidified before SS. Liquid Fe/Ni spread well on the skin of solid-state W [37]. Thus, liquid Fe/Ni could completely encapsulate the pre-solidified W particles. These explained the lack of cracks and pores around the solidified W particles.

Tiny liquid W droplets contained less heat than large W droplets; hence tiny W droplets cooled faster than large W droplets. The surface tension of the liquid increased as the temperature dropped. As a result, the small W droplets first agglomerated into spherical particles due to the smallest Gibbs surface free energy [38]. The large W droplets did not have time to completely solidify before the surrounding liquid SS solidified; as a result, the large W droplets finally solidified into embedded irregularly-shaped particles.

The magnified SEM image of this interface (figure 3(c2)) provided more clues to revealing the above phenomena, which provided the trajectory of the W droplets in the remelted SS melt pool. As shown in arrows in figure 3(c2), regardless of the size of the W droplets, the angle between the falling direction of all W droplets in the melt pool and the laser scanning direction was 153°. It may result from the combined force of gravity and the movement of the melt pool caused by laser scanning. Behind the small W droplet, an area (marked by dotted lines in figure 3(c2)) similar to the tail of a meteor appeared. The microstructure of this area (bright dots (W) on the dark background (SS)) was different from those of solidified W and SS. We speculated that W droplets reacted with liquid SS while falling in the melt pool and formed new Fe–W/Ni–W phases. This speculation was confirmed by subsequent XRD and EBSD test results.

4.2. EDS mapping of the material interfaces

4.2.1. Element diffusion at the SS→W interface. As shown in figure 4(a1), we did not find a bowl-shaped element mixing area caused by the Marangoni convention-induced circular flow in the melt pool [39]. It indicated that the pre-printed W part was not remelted during the LPBF printing of the SS part.

On the other hand, it was observed that weak signals of Ni and Fe diffused to the W side (figures 4(a3) and (a4)). The EDS line scanning plot (figure 4(a5)) based on the red scan path in figure 4(a1) provided more information on this solid-state diffusion (SSD) phenomenon. As shown by the yellow arrow and the red arrow in figure 4(a5), at the material interface, the element content of W increased and the element contents of SS decreased gradually, rather than a sharp change. It is a typical concentration profile of steady-state inter-diffusion caused by the Kirkendall effect [40]. The width of the mutual diffusion zone was around 0.6 μm, which was similar to that in the previous study [41]. As highlighted by the black arrow in figure 4(a5), the total diffusion depth of the elements in SS on the W side exceeded 20 μm.

The movement or flux of the elements (J) in SSD is proportional to the element diffusion coefficient (D) and the element concentration gradient ($\frac{dC}{dx}$), according to the Fick's first law of diffusion $\left(J = -D\frac{dC}{dx}\right)$ [42]. The diffusion coefficient of Ni–W is much greater than that of the Fe–W (6×10^{-15} m^2 s^{-1} for Ni–W [43], 10^{-18} m^2 s^{-1} to 6×10^{-19} m^2 s^{-1} for Fe–W [44]). Therefore, the diffusion of Ni into the solid-state W area is stronger than that of Fe.

The research of Reisner *et al* [44] reported that the diffusion coefficient is directly proportional to temperature. Although the laser energy density for melting SS could not remelt the surface of pre-printed W layers, it could keep the printed part at high temperature, increase the active energy of Ni and Fe elements and let them migrate to the W side via SSD and archive the SS→W interface bonding.

In this study, we observed that the diffusion of W via SSD was less than that of Ni and Fe, because the body-centred cubic (BCC) grain structure of W requires higher activation energy than the face-centred cubic (FCC) structure to achieve SSD [45]. Besides, the atomic density and diameter of the W element are higher and bigger, which also lead to higher active energy. Therefore, under the same processing conditions, the jump frequency of W atoms is lower than that of Ni/Fe [46], so the SSD-induced diffusion of W was less than that of Ni and Fe in this investigation.

4.2.2. Element distribution at the W→SS interface. The area between the two red dashed lines in figure 4(b1) was the collapsed W layer close to the W→SS interface. By comparing the EDS map of W (figure 4(b2)) with the EDS maps of Fe/Ni (figures 4(b3) and (b4)), we found that the W element shed from the bottom of the W layer widely diffused in the remelted SS layers. In addition, the Fe/Ni EDS maps (figures 4(b3) and (b4)) showed that there was an SS layer above the collapsed W layer (the area between the two red dashed lines in figures 4(b3) and (b4)). The thickness of this SS layer was uneven, and there were two tips with a spacing of 100 μm, as shown in figure 4(b3). This distance value was the same as the laser scanning hatch distance for processing W in this study. Therefore, these two tips were likely to be keyhole tips.

The EDS line scanning result (figure 4(b5)) was based on the red scan path shown in figure 4(b1). The scan path was divided into six regions (marked by R1 to R6 in figure 4(b5)). The bright regions (R1, R3, R5) were mainly distributed with W, and no obvious SS element signals were detected. In the dark regions (R2, R4, R6), strong W signal and SS element

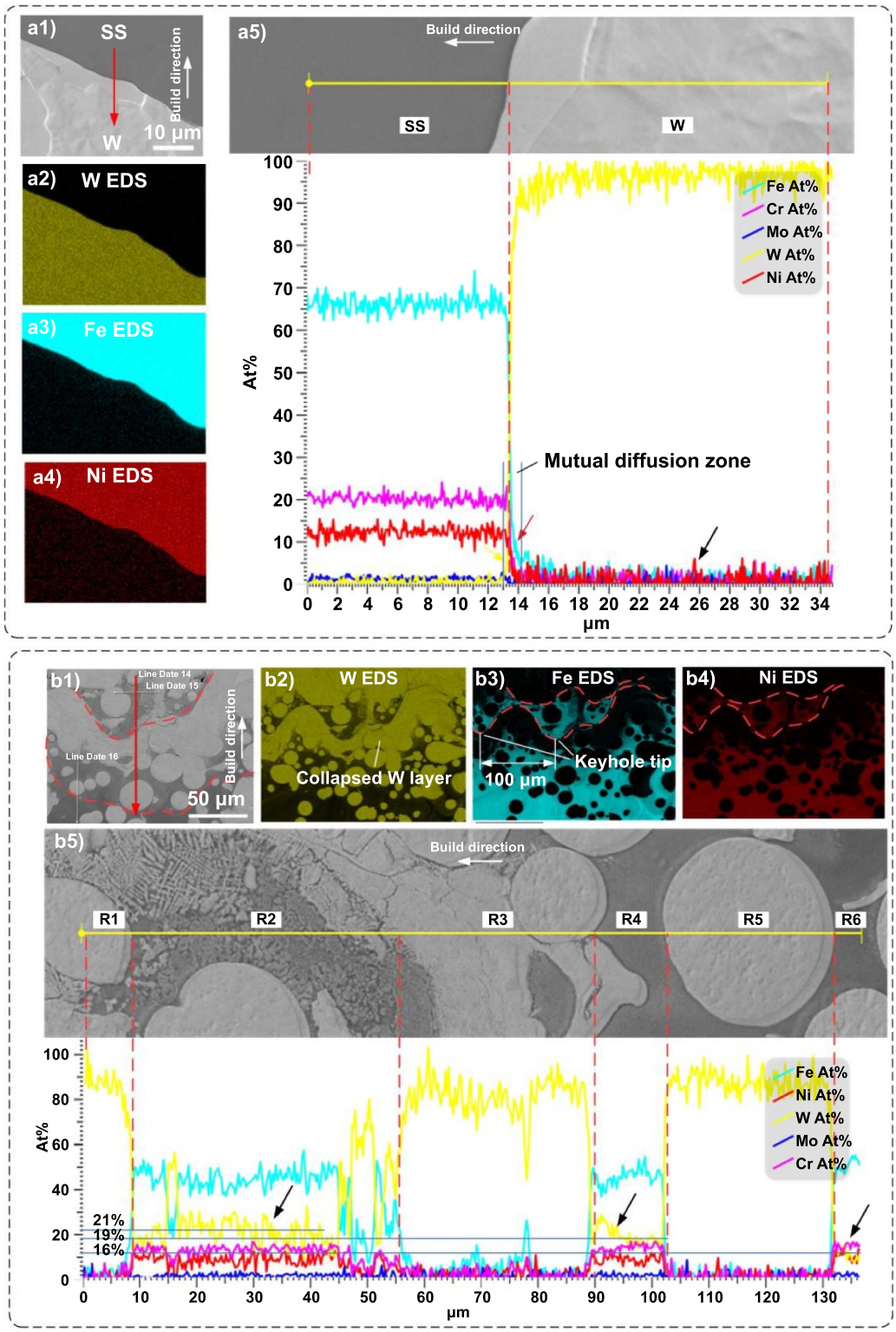

Figure 4. (a1), (b1) SEM micrographs of different material interface; (a2)–(a4) and (b2)–(b4) show corresponding element EDS maps; (a5), (b5) present the EDS line scanning plots according to the scanning paths in (a1), (b5).

signals were observed, indicating that W diffused into the initial SS regions. A large amount of W diffusion increased the possibility of forming the W–Fe/Ni intermetallic phases. It was notable that along the build direction, the mean values of W content of these element mixing regions gradually increased (16 At% for R6, 19 At% for R4, and 21 At% for R2). It may be due to that the melted W in R2 was near the upper W molten pool, so the concentration of liquid-phase W was higher. According to Fick's first law, a higher concentration gradient causes more elements to diffuse. Besides, compared

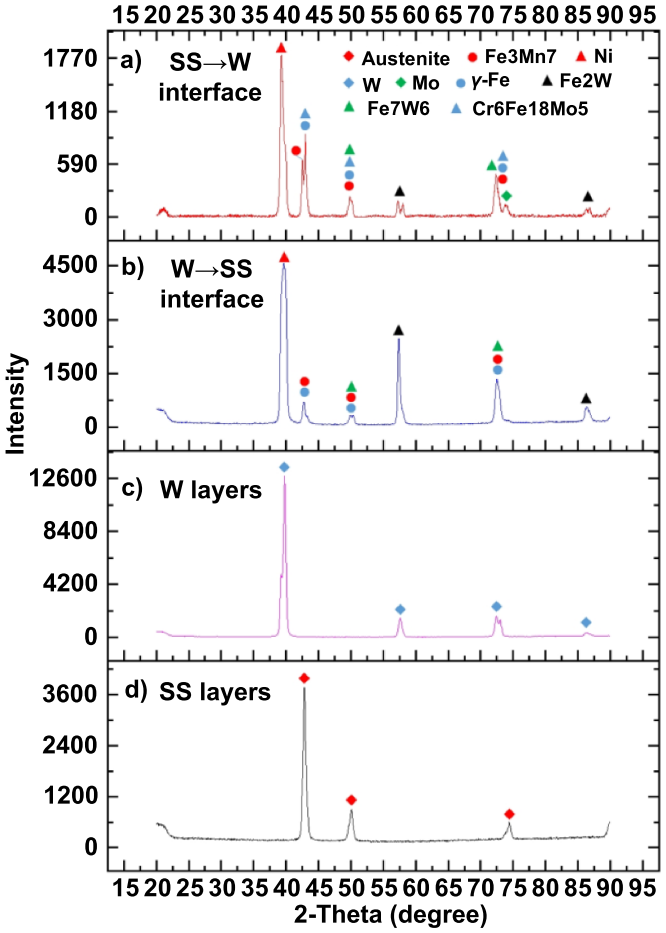

Figure 5. XRD patterns of different regions on the SS–W–SS sandwich sample.

to the liquid W in R6, the liquid W in R2 should be hotter due to the shorter distance to the upper W melt pool; Higher temperature contributed to stronger element diffusion [44].

4.3. XRD of material interfaces

As shown in figure 5(d), a typical XRD pattern of the single γ-austenite FCC structure was observed at the SS part, similar to that of LPBF-printed SS reported in a previous study [47]. Four major peaks in the diffraction pattern (figure 5(c)) of the LPBF-printed W region was the same as the original pure BCC W powder [48].

The XRD patterns at the two material interfaces (figures 5(a) and (b)) showed a significant difference compared with the above two base materials. New phases composed of elements in SS appeared at both two interfaces, such as Ni, Mo, Fe_3Mn_7, and $Cr_6Fe_{18}Mo_5$; it indicated the decomposition of SS under the high laser energy density. Fe from SS reacted with W and led to secondary phases, including Fe_2W and Fe_7W_6. It was worth noting that the XRD peak intensities of new Fe–W phases at the W→SS interface were significantly higher than those at the SS→W interface. The XRD test conditions remained unchanged in this study, so the difference in XRD intensity should be caused by the phase concentration at the two interfaces. The high laser energy density for melting W caused the top surface of the pre-cured SS to be remelted, as presented in figure 3(b6); many W droplets fell into the remelted SS, significantly increasing the element reaction area, and resulting in more Fe–W phases formed.

All these new phases detected by XRD were considered as candidates in the following EBSD phase mapping.

4.4. EBSD of the material interfaces

4.4.1. Micro-texture at the SS→W interface. Both LPBF-printed base materials presented columnar phases, see figure 6(a1). The cracks along the build direction only appeared on the W side, as highlighted by arrows in in figure 6(a1). It may be due to that the ductile–brittle transition temperature of W (500–700 K) is low [35], causing stress concentration and cracks during LPBF processing [49].

The grain size distribution of figure 6(a1), calculated by the HKL Tango software, showed that the average grain size of SS (mean: 98.428 μm^2, number of grains: 754) was smaller than that of W (mean: 212.41 μm^2, number of grains: 141). As mentioned in section 4.1.1, the crystal grains produced by LPBF grow along the building direction. The SS fine-grained structure in figure 6(a1) appeared in the newly printed layers close to the SS→W interface. The larger W grains were those after printing to a thickness of 2 mm, and the W grains at this position had grown. Hence, it was normal that the newly-formed SS grains shown in figure 6(a1) were smaller than the grown W grains.

The phase map (figure 6(a3)) indicated that the SS–W interface mainly consisted of Fe-FFC, W, and Ni_4W phases. Notably, the Ni_4W phase was just presented at the SS grain boundaries, for instance, the region marked by R1 in figures 6(a1) and (a3). It should be resulted from the diffusion of W upward due to the grain boundary diffusion (GBD). GBD is the most common solute migration path in polycrystalline materials. The diffusion of elements in the solid metal along the grain boundary is faster and easier than the solid diffusion through the grain lattice [50], which can occur at low and medium temperatures. The more grain boundaries, the more elements migrate through GBD, which will result in higher interface bonding strength [51]. In this study, the grain boundaries on the SS side were far more than those on the W side. Therefore, it was observed that many W migrated to the SS grain boundaries through GBD. The high temperature caused by LPBF made the diffused W react with Ni to generate Ni_4W.

4.4.2. Micro-texture at the W→SS interface. An EBSD examination was carried out on the EDS mapping area (figure 4(b1)) and its surrounding area.

As shown in the red box in figure 6(b1), the initial microstructure of pre-printed SS was comprised of fine columnar grains. The high energy for melting W caused the top surface of SS to be remelted and recrystallized (see the red circle in figure 6(b1)). There were many spherical and irregular shaped W particles embedded in these new SS grains without defects

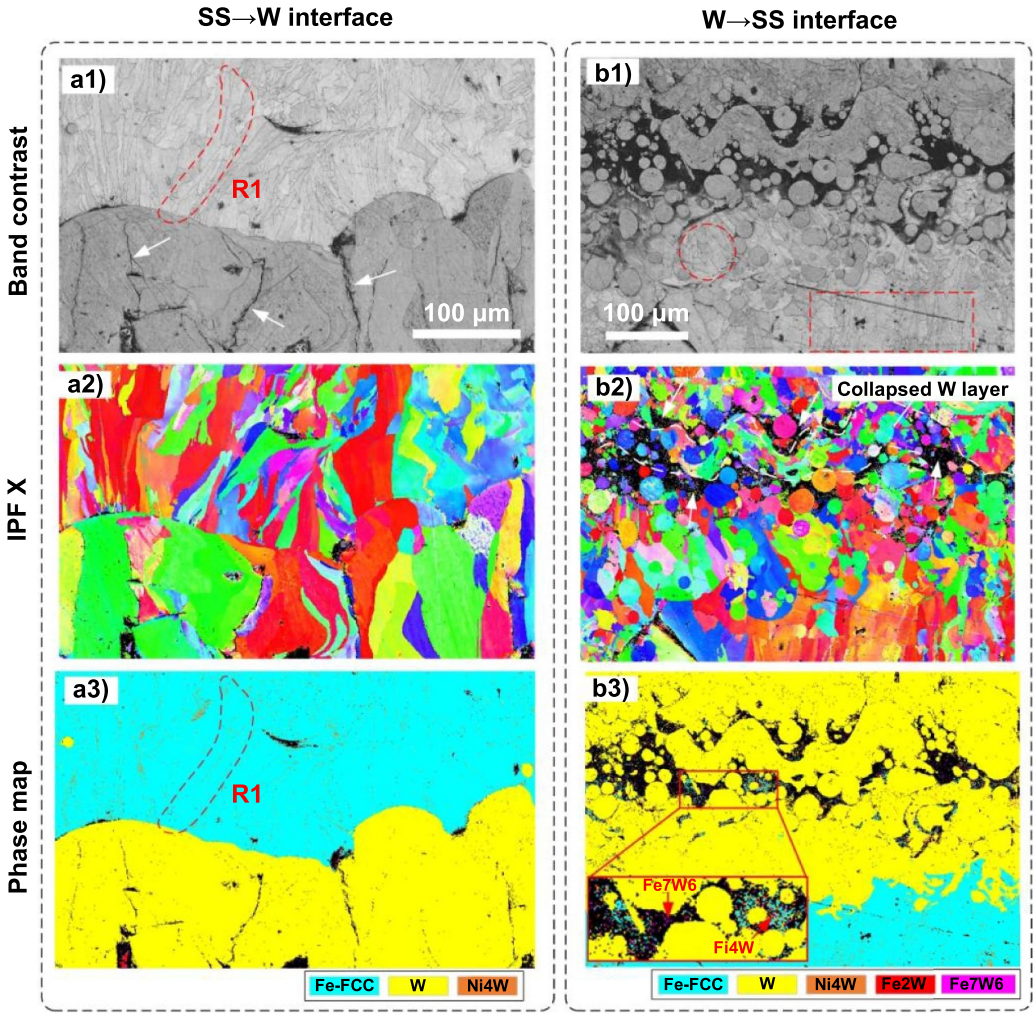

Figure 6. (a1)–(a3) and (b1)–(b3) are the band contrast map, inverse pole figure, and phase map at two material interfaces, respectively.

such as pores/cracks. It proved that liquid W solidified earlier than liquid SS.

The grain type of the W–SS mixing zones distributed on both sides of the collapsed W layer could not be identified via EBSD and was displayed in black, see the area pointed by the arrows in figure 6(b2). The phase map indicated that intermetallic phases, including Ni_4W/Fe_2W/Fe_7W_6, appeared in these element mixing zones, as marked by arrows in figure 6(b3).

4.5. Nano-hardness and elastic modulus of the material interfaces

Figures 7(a) and (b) present the original data of nano-hardness at different locations on the sample and that of measured reduced elastic modulus (E_r) via the nanoindentation method. The elastic modulus of test region (E_1) was converted from the measured E_r based on the formula (1) mentioned in the article [52], and shown in figure 7(b):

$$\frac{1}{E_r} = \frac{1-v_1^2}{E_1} + \frac{1-v_2^2}{E_2}. \quad (1)$$

In which, v_1 is the Poisson's ratio. In this study, we set the Poisson's ratio of the SS region to 0.27, and the Poisson's ratio of the material in the other areas was set to 0.3; v_2 and E_2 are the Poisson's ratio (0.07) and the modulus of elasticity (1141 GPa) of the diamond indenter, respectively.

4.5.1. Nano-hardness. Compared with the data of bulk materials produced by conventional methods, as shown in table 3, LPBF-printed base materials in this study always presented significant higher nano-hardness. For example, the hardness of the SS area in this study was 1.86 times that of the bulk 316L, and the hardness of the W area was 1.55 times that of the bulk W. It might be due to the fine-grained structure produced by rapid cooling cycles in the LPBF process [53]. Because of the finer metal grains, the total area of grain boundaries was larger; it led to more dislocation barriers and higher resistance to plastic deformation of the metal during the hardness test [54].

As shown in figure 7(a), the SS→W interface had similar hardness compared with the SS base (6.20 and 5.38 GPa respectively). But the hardness of the W base (8.99 GPa) was

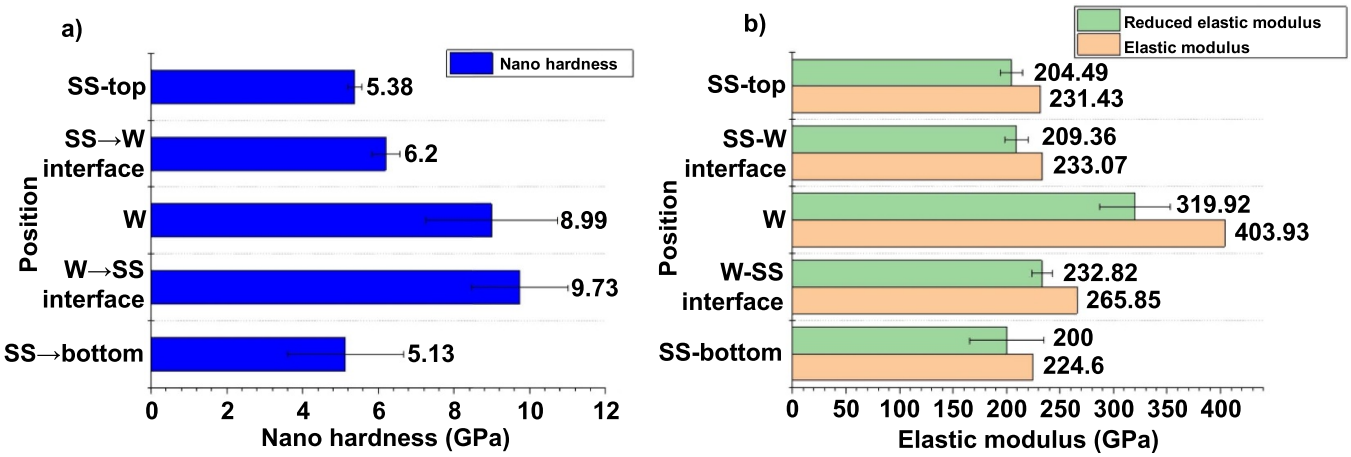

Figure 7. (a) Nano hardness plot of the SS–W–SS sandwich structure and (b) the corresponding plot of reduced elastic modulus and elastic modulus.

Table 3. Nano-hardness and elastic modulus of the bulk 316L SS and bulk W reported in the literature.

	Nano-hardness	Elastic modulus	References
Bulk 316L SS	2.90 GPa	220.40 GPa	[55]
Bulk W	5.80 GPa	410.00 GPa	[56]

much higher than that of this interface. As mentioned earlier, there was no remelting of the pre-printed W at this material interface. Only small volume of Ni/Fe elements migrated to the solid W region. As a result, there was very few high-hardness intermetallic phase produced.

On the other hand, the W→SS interface showed a nano hardness as high as 9.73 GPa, which exceeded the hardness of W (8.99 GPa). It should be due to that a large amount of W was incorporated into the pre-printed SS, and the result of the formation of high brittleness Fe–W/Ni–W intermetallic phases as shown in figure 6(b3).

4.5.2. Elastic modulus. The data in figure 7(b) and table 3 revealed that the elastic modulus of the SS region and the W region in this study were similar to the elastic modulus of the material processed by the traditional methods.

The elastic modulus of the SS→W interface (233.07 GPa) and that of the W→SS interface (265.85 GPa) were both between that of the SS regions (231.43/224.60 GPa) and that of the W region (403.93 GPa). It should result from a small amount of W with the high elastic modulus infiltrating into the SS matrix with the low elastic modulus.

In summary, the hardness and elastic modulus of the SS→W interface were similar to that of the SS base. The W→SS interface combined the characteristics of the higher hardness of W and the relative lower elastic modulus of SS.

5. Melt pool fluid dynamics in multiple material interfaces

5.1. Morphologies of melted powder layers

5.1.1. Morphology of the SS→W interface. A continuous melted SS track is presented in figure 8(a1), indicating that SS has good wettability with the W substrate. The clear interface in figure 8(a2) showed that the W base was not melted, and no element mixing occurred.

5.1.2. Morphology of the W→SS interface. As presented in figure 8(b1), it was interesting that SS instead of W appeared on skin of the melted W track. The high energy density resulted in the keyhole mode. Figure 8(b2) clearly presented that W flew into the SS cavity and the formation of pores; the latter is a typical defect of the keyhole mode in LPBF [57]. The keyhole depth filled with W reached 88.93 μm, which was shallower than the deepest position discovering W in the experiment (>130 μm, figure 3(b6)). An explanation will be given in section 6.2. The 3D morphology of the entire W powder layer after laser melting (figure 8(b3)) revealed that W sunk into the SS base while SS floated to the top. This simulation result was similar to that of the SS region on the top of the W layer observed in the EDS maps (figures 4(b3) and (b4)). We will discuss the cause of this phenomenon in detail in section 6.2.

5.2. Melt pool temperature distribution at the material interfaces

The molten pool temperature contours of the two material interfaces in the '300–1658 K' range are shown in figures 9(a1) and (b1) respectively; and those in the '300–3695 K' range are shown in figures 9(a2) and (b2) respectively. 1658 and 3695 K are the solidus temperature of 316L SS and W, respectively, as presented in table 2.

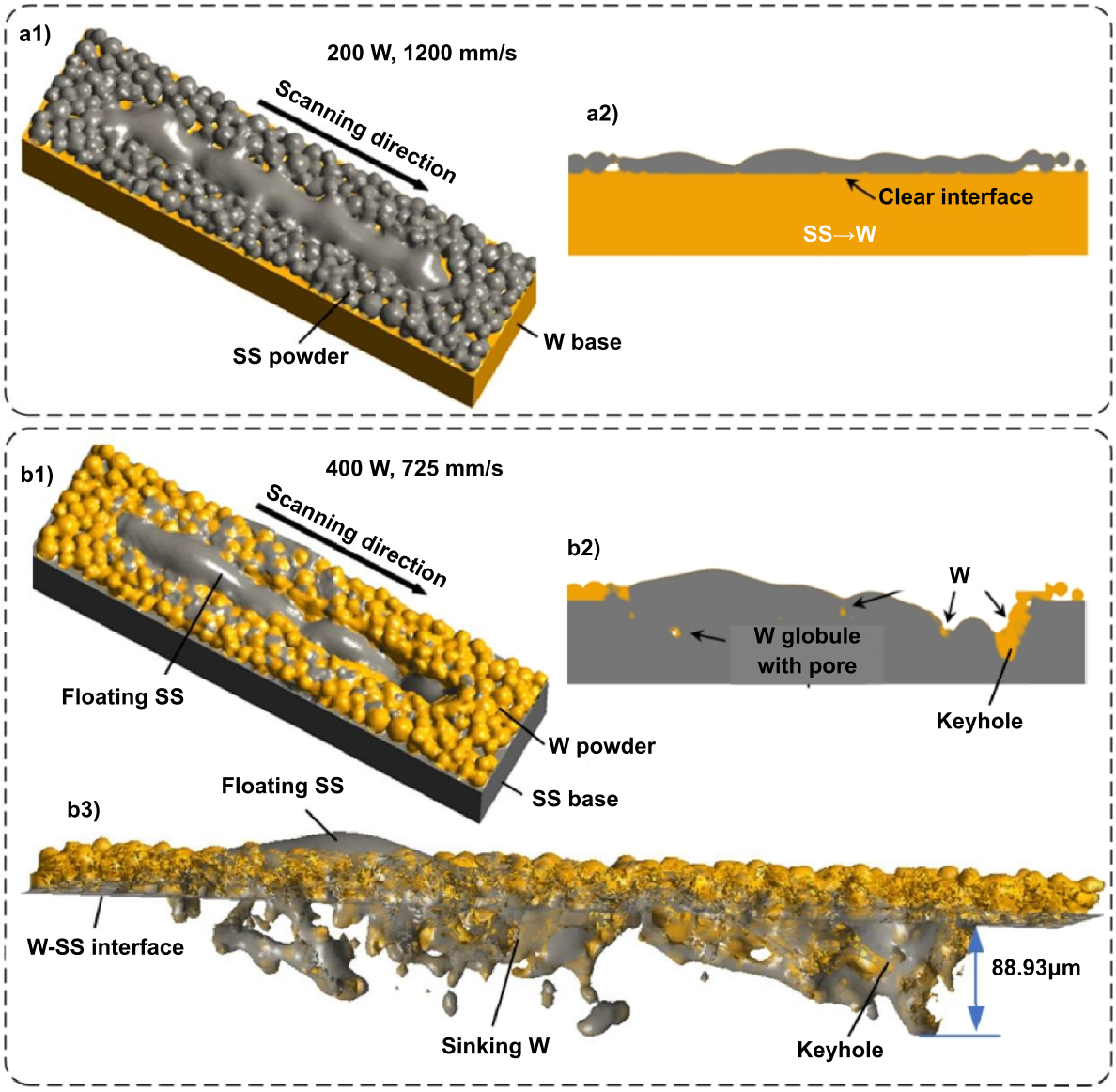

Figure 8. (a1) Scanned track morphology of SS powder layer at the SS→W interface and (a2) its cross-section; (b1) the scanned track morphology of W powder layer at the W→SS interface and (b2) its cross-section, (b3) 3D morphology of the melted W powder layer.

5.2.1. Melt pool temperature profile at the SS→W interface. The melt pool depth of SS achieving the melting point of SS (1658 K) was only 32.65 μm, see figure 9(a), slightly greater than the SS powder layer thickness (30 μm in this study). The heat in the molten pool dissipated quickly through heat conduction of the W base because of its good thermal conductivity. Besides, the molten pool depth with a temperature no less than the W melting temperature (3695 K) was only 20.26 μm (figure 9(a2)), lower than the powder layer thickness. It was clear that the low laser energy density (79.37 J mm^{-3}) for melting SS could only melt a single layer of SS powder. It was impossible to remelt the surface of the W base and further lead to element mixing inside in the molten pool.

5.2.2. Melt pool temperature profile at the W→SS interface. The high energy density for melting W powder layer (183.91 J mm^{-3}) resulted in the keyhole mode (see figure 9(b1)), which not only melted the 30 μm thick W powder layer, but also deeply remelted the SS substrate; the molten pool depth with temperature greater than the melting point of SS was 127.49 μm. As shown in figure 9(b2), the region where the temperature reached the melting point of W was the front of the melt pool, which caused the liquid W to flow into the keyhole cavity. As mentioned earlier, the SS base was also deeply melted. Therefore, the liquid W could mix and react with the elements (i.e. Ni, Fe) in the liquid SS.

5.3. Melt pool velocity field at the W→SS interface

Despite having negative surface tension coefficients (table 2) for both W and SS materials, the velocity distribution in the laser beam centre presented a downward flow attributed to the high recoil pressure induced by keyhole formation, as shown in figure 10(a). Consequently, the melted W in the melt pool

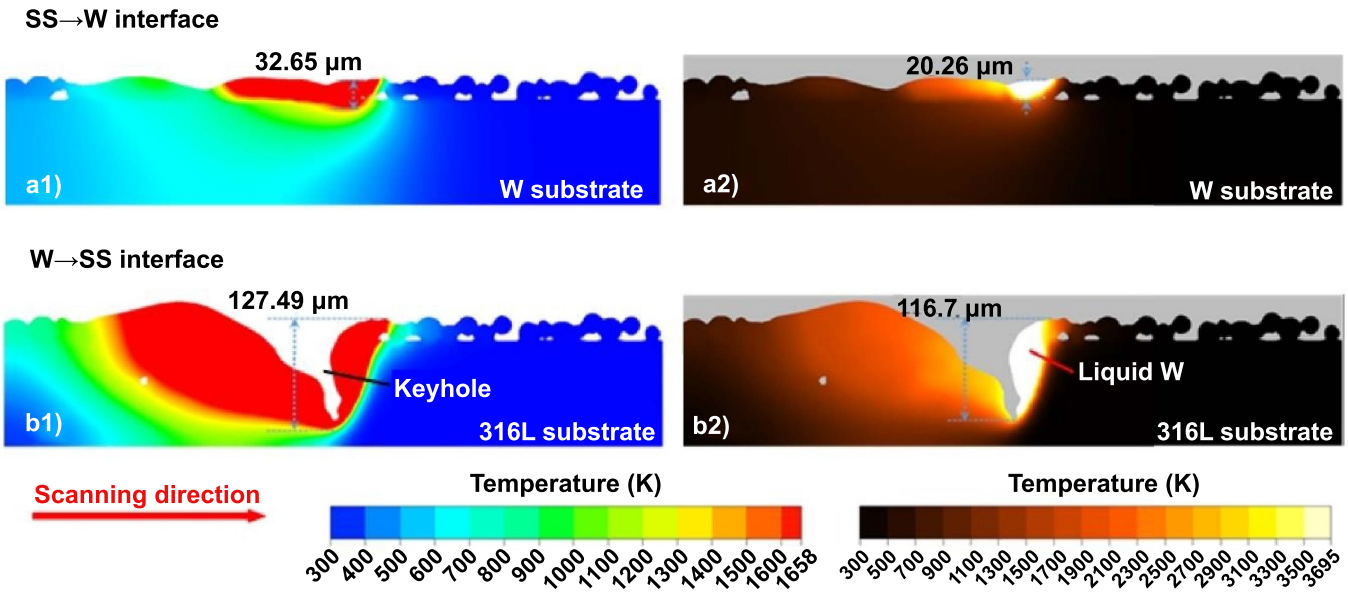

Figure 9. Melt pool temperature profiles at the SS→W interface in the range (a1) 300 °C–1658 °C and (a2) 300–3695 K; melt pool temperature profiles at the W→SS interface in the range (b1) 300 °C–1658 °C and (b2) 300–3695 K.

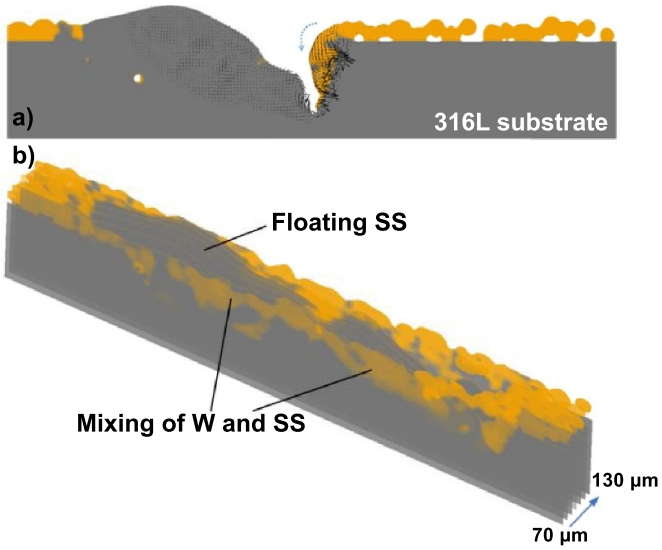

Figure 10. (a) Melt pool velocity field at the W→SS interface along the longitudinal cross-section, and (b) stacked views of simulated cured W→SS interfaces with different longitudinal sections (position 70–130 μm).

front would tend to flow towards the bottom of the keyhole cavity with the combined effects of surface tension forces, recoil pressure and gravity, as illustrated in figure 10(b). The Marangoni convection in the molten pool led to the rapid evolution of the fluid flow [58]; the W phase mixed with liquid SS at the subsurface of the SS base (figure 10(b)). W have higher density and higher thermal conductivity compare with SS, so the W phase first solidified in the melt pool and sank due to gravity [59], leading to element segregation. The compressibility of liquid metal is poor [60] (i.e. the total volume of W and SS participating in the reaction was almost unchanged), so falling W particles occupied the space of SS located initially below. Subsequently, liquid SS was forced to float up and brought back to the top of the melt pool through circulating flows and solidified there. This melt pool behaviour should be the cause why we observed SS instead of W on the initial W scanning track (figure 8(b1)). The above-mentioned ups-down migration of elements takes time to complete, so we only found a completely floating SS at the beginning of the scanning track that melted and solidified first.

6. Discussion of interfacial bonding mechanisms

We proposed the following dissimilar material interfacial bonding mechanisms according the above experimental results and simulation results.

6.1. Bonding mechanism at the SS→W interface

Figure 11(a) illustrates the bonding mechanism at the SS→W interface. When laser melting SS on the W surface, the melt pool depth caused by the laser irradiation cannot melt the pre-printed W (figures 3(b5), (c1) and 8(a2)). However, at high temperature and argon environment, the wettability of liquid Fe/Ni is good on the solid-state W surface [37], hence liquid Fe/Ni can spread into a thin layer without warping and balling phenomena at the SS→W interface. It is a prerequisite for the subsequent occurrence of SSD and GBD phenomena. In this study, SSD and GBD are the fundamental mechanisms to achieve SS→W interface bonding without melting W.

In the presence of material concentration gradients [42] and high-temperature heating to increase the activation energy of atoms [61], SSD can occur in solid metals. The sharp SS→W interface in this investigation provided the material concentration gradient required by SSD. Meanwhile, during LPBF processing, the laser beam repeatedly scanned the powder bed to maintain the powder bed at a high temperature, despite

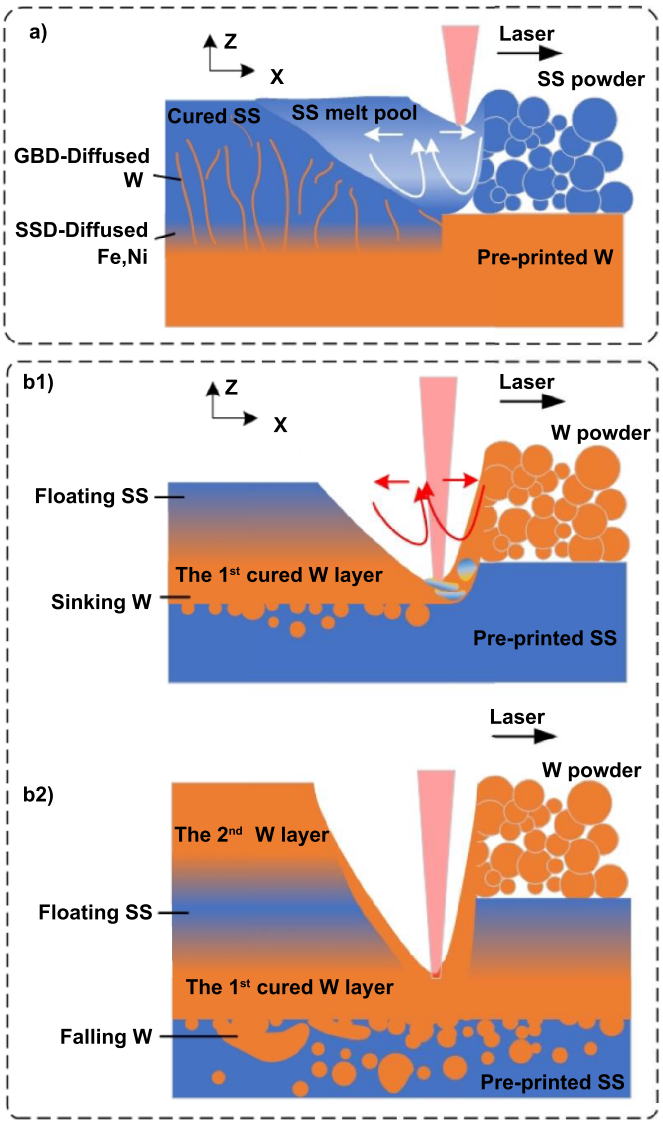

Figure 11. (a) The schematic of the SS→W interfacial bonding mechanism; the schematics of the W→SS interfacial bonding mechanism when (b1) fusing the first W powder layer and (2) melting the second W powder layer.

temperature fluctuations. Hence, bonding SS to W via LPBF met the two requirements of SSD, so Ni and Fe with high diffusion coefficients migrated to the W side (figure 5(a5)). Due to the high activation energy of solid W, much less W migrated to the SS side via SSD (figure 5(a5)).

On the other hand, the activation energy required for GBD through grain boundaries is much lower than the activation energy required for SSD through grain lattices [62]. Metals with more grain boundaries are more prone to GBD [63]. The SS in this study presented fine columnar grains with many grain boundaries spreading along the build direction (figure 6(a1)). Therefore, W with low activation energy could migrate to the SS side through GBD (figure 6(a3)). Because of the powder-bed's high temperature caused by repeated laser irradiation, the migrated W reacted with Ni and Fe to produce new phases (i.e. Ni_4W in figure 6(a3)).

6.2. Bonding mechanism at the W→SS interface

The keyhole-mode molten pools during printing the first W layer and the second W layer made W to bond to the pre-printed SS base.

6.2.1. Printing the first W layer. The simulation result showed that the high laser energy for melting W caused the melt pool at the material interface to become an excessive keyhole mode (figure 8(b2)). The pre-printed low melting point SS base was melted and evaporated due to that the boiling temperatures of Ni and Fe in SS (2913 °C and 2862 °C) are lower than the W melting temperature (3422 °C). The SS evaporation process generated a recoil pressure on the SS molten pool's liquid surface. Subsequently, the recoil pressure deformed the above-mentioned liquid surface and pushed the liquid material in the SS melt pool sidewards, allowing the laser beam to penetrate to a deeper liquid–gas interface inside the pre-printed SS layers, and ultimately resulted in the deep SS keyhole cavity [64], as shown in figure 9(b1). The liquid W flew into and filled the keyhole cavity (figure 9(b2)). During such a process, the liquid W was continuously mixed with the liquid SS (figure 10(a)) and solidified before the liquid SS (figure 6(b1)) and finally embedded in the SS matrix (figure 10(b)). Meanwhile, the low-density liquid SS was carried by the melt pool circulating flows to the molten pool's top surface and solidified, forming a thin layer of floating SS (figures 4(b3), (b4) and 8(b1)). According to the simulation result, the depth of the melted SS subsurface layer (i.e. the thickness of the SS layer embedded with W particles) was 88.93 μm.

The above bonding mechanism is illustrated in figure 11(b1).

6.2.2. Printing the second W layer. During printing the second layer of W, the high energy density again led to the keyhole-mode molten pools; the keyhole tips penetrated into the solidified first W layer (figure 4(b3)). The good thermal conductivity of W caused a large amount of heat in the W melt pool was quickly transferred to the underlying SS layers. The solidified SS layers were remelted for the second time, which further caused the solidified first W layer to collapse. Many W particles, including large ones with irregular shapes, fell from the bottom of the first W layer and gradually sunk in the liquid SS, which made the thickness of the SS layers embedded with W particles reach over 130 μm (figure 3(b6)). Falling W droplets continuously mixed and reacted with the liquid Fe/Ni (figures 3(c2) and 4(b5)) to produce intermetallic phases such as Ni_4W and Fe_2W (figure 6(b3)).

The above bonding mechanism is illustrated in figure 11(b2).

7. Conclusion

A SS→W→SS sandwich structure was additively manufactured using a multi-material LPBF technology. The material characterization results indicated that the morphology, element distribution, phase distribution, hardness at the two

material interfaces were significantly different. Modelling and simulation tool were used to reveal the molten pools' thermodynamic behaviour and their temperature distribution during laser melting the above two material interfaces. Two material interfaces' metallurgical bonding mechanisms in the multiple material LPBF process were proposed based on the above experimental and simulation results.

The experimental and the simulation results show verified that the pre-printed W base cannot be re-melted by the laser energy for printing SS. Fortunately, Ni and Fe with low activation energy migrates to the W side through SSD. In addition, W with high activation energy migrates to the SS side through GBD. These two diffusion phenomena contribute to the bonding of SS and W. No secondary phase is found on the W side, and the Ni_4W phase is widely observed at the SS grain boundaries. The SS→W interfacial hardness (6.2 GPa) is similar to that of SS and much lower than that of W. Its elastic modulus (233.07 GPa) is between SS and W.

This study shows that the high energy for melting W causes molten pools at the W→SS interface to enter an excessive keyhole mode. The keyhole tips deeply penetrate into the pre-printed SS base. The liquid W with high density in the melt pool flows into the keyhole cavity, sink in the liquid SS, and is finally embedded in the SS matrix. The low-density SS is forced to float up, forming a thin layer above the W scanning track. In the above process, the liquid W mixes and reacts with the liquid SS, resulting in secondary phases (Ni_4W, Fe_2W, Fe_6W_6). These new phases cause the nano-hardness of the SS→W interface to be higher than that of W (9.73 and 8.99 GPa, respectively). The elastic modulus of the SS→W interface (265.85 GPa) is between those of SS and W.

This research may apply to the AM of W–SS bimetallic components used in the nuclear industry. After revealing their interfacial bonding mechanisms, the subsequent investigation will optimize the process parameters, especially suitable laser energy density at the material interface [65], to improve the mechanical performance of the real W–SS bimetallic components fabricated via multi-material LPBF.

Acknowledgments

This investigation was funded by the Engineering and Physical Science Research Council (EPSRC), UK (Grant Nos. EP/P027563/1 and EP/M028267/1), the Science and Technology Facilities Council (STFC) (Grant No. ST/R006105/1), and the Bridging for Innovators Programme of Department for Business, Energy and Industrial Strategy (BEIS), UK.

ORCID iD

Chao Wei https://orcid.org/0000-0003-4419-9093

References

[1] Zhang J, Luo L M, Zhu X Y, Chen H Y, Chen J L, Zan X, Cheng J G and Wu Y C 2015 Effect of doped Lu_2O_3 on the microstructures and properties of tungsten alloy prepared by spark plasma sintering *J. Nucl. Mater.* **456** 316–20

[2] Şahin Y 2014 Recent progress in processing of tungsten heavy alloys *J. Powder Technol.* **2014** 764306

[3] Waseem O A and Ryu H J 2016 Tungsten-based composites for nuclear fusion applications *Nuclear Material Performance* ed R A Rahman (London: IntechOpen) (https://doi.org/10.5772/62434)

[4] Senthilnathan N, Annamalai A R and Venkatachalam G 2018 Microstructure and mechanical properties of spark plasma sintered tungsten heavy alloys *Mater. Sci. Eng.* A **710** 66–73

[5] Zu Y S and Lin S T 1997 Optimizing the mechanical properties of injection molded W4.9%Ni2.1%Fe in debinding *J. Mater. Process. Technol.* **71** 337–42

[6] Iveković A, Montero-Sistiaga M L, Vanmeensel K, Kruth J-P and Vleugels J 2019 Effect of processing parameters on microstructure and properties of tungsten heavy alloys fabricated by SLM *Int. J. Refract. Met. Hard Mater.* **82** 23–30

[7] Bose A *et al* 2018 Traditional and additive manufacturing of a new Tungsten heavy alloy alternative *Int. J. Refract. Met. Hard Mater.* **73** 22–28

[8] Cai Q S, Liu W S, Ma Y Z and Liu H Y 2015 Microstructure, residual stresses and mechanical properties of diffusion bonded tungsten-steel joint using a V/Cu composite barrier interlayer *Int. J. Refract. Met. Hard Mater.* **48** 312–7

[9] Park J Y, Jung Y I, Choi B K, Lee D W and Cho S 2013 Joining of tungsten to ferritic/martensitic steels by hot isostatic pressing *J. Nucl. Mater.* **442** S541–5

[10] Wei C, Li L, Zhang X Y and Chueh Y-H 2018 3D printing of multiple metallic materials via modified selective laser melting *CIRP Ann.* **67** 245–8

[11] Chadha K, Tian Y, Pasco J and Aranas C Jr 2021 Dual-metal laser powder bed fusion of iron- and cobalt-based alloys *Mater. Charact.* **178** 111285

[12] Goh G L, Zhang H N, Chong T H and Yeong W Y 2021 3D printing of multilayered and multimaterial electronics: a review *Adv. Electron. Mater.* **7** 2100445

[13] Wei C and Li L 2021 Recent progress and scientific challenges in multi-material additive manufacturing via laser-based powder bed fusion *Virtual Phys. Prototyp.* **16** 347–71

[14] Wei C, Zhang Z Z, Cheng D X, Sun Z, Zhu M H and Li L 2021 An overview of laser-based multiple metallic material additive manufacturing: from macro- to micro-scales *Int. J. Extrem. Manuf.* **3** 012003

[15] Tan C L, Zhou K S and Kuang T C 2019 Selective laser melting of tungsten-copper functionally graded material *Mater. Lett.* **237** 328–31

[16] Wei C, Sun Z, Chen Q, Liu Z and Li L 2019 Additive manufacturing of horizontal and 3D functionally graded 316L/Cu10Sn components via multiple material selective laser melting *J. Manuf. Sci. Eng.* **141** 081014

[17] Wang D Z, Yu C F, Zhou X, Ma J, Liu W and Shen Z J 2017 Dense pure tungsten fabricated by selective laser melting *Appl. Sci.* **7** 430

[18] Field A C, Carter L N, Adkins N J E, Attallah M M, Gorley M J and Strangwood M 2020 The effect of powder characteristics on build quality of high-purity tungsten produced *via* laser powder bed fusion (LPBF) *Metall. Mater. Trans.* A **51** 1367–78

[19] Iveković A, Omidvari N, Vrancken B, Lietaert K, Thijs L, Vanmeensel K, Vleugels J and Kruth J-P 2018 Selective laser melting of tungsten and tungsten alloys *Int. J. Refract. Met. Hard Mater.* **72** 27–32

[20] Casati R, Lemke J and Vedani M 2016 Microstructure and fracture behavior of 316L austenitic stainless steel produced by selective laser melting *J. Mater. Sci. Technol.* **32** 738–44

[21] Chen K Y, Wang C, Hong Q F, Wen S F, Zhou Y, Yan C Z and Shi Y S 2020 Selective laser melting 316L/CuSn10 multi-materials: processing optimization, interfacial characterization and mechanical property *J. Mater. Process. Technol.* **283** 116701
[22] Wang D, Song C H, Yang Y Q and Bai Y C 2016 Investigation of crystal growth mechanism during selective laser melting and mechanical property characterization of 316L stainless steel parts *Mater. Des.* **100** 291–9
[23] Chen J, Yang Y Q, Song C H, Zhang M K, Wu S B and Wang D 2019 Interfacial microstructure and mechanical properties of 316L/CuSn10 multi-material bimetallic structure fabricated by selective laser melting *Mater. Sci. Eng.* A **752** 75–85
[24] Caiazzo F, Alfieri V and Casalino G 2020 On the relevance of volumetric energy density in the investigation of Inconel 718 laser powder bed fusion *Materials* **13** 538
[25] Gu H, Wei C, Li L, Ryan M, Setchi R, Han Q Q and Qian L L 2021 Numerical and experimental study of molten pool behaviour and defect formation in multi-material and functionally graded materials laser powder bed fusion *Adv. Powder Technol.* **32** 4303–21
[26] Gu H, Wei C, Li L, Han Q Q, Setchi R, Ryan M and Li Q 2020 Multi-physics modelling of molten pool development and track formation in multi-track, multi-layer and multi-material selective laser melting *Int. J. Heat Mass Transfer* **151** 119458
[27] Tang C, Tan J L and Wong C H 2018 A numerical investigation on the physical mechanisms of single track defects in selective laser melting *Int. J. Heat Mass Transfer* **126** 957–68
[28] Tolias P and The EUROfusion MST1 Team 2017 Analytical expressions for thermophysical properties of solid and liquid tungsten relevant for fusion applications *Nucl. Mater. Energy* **13** 42–57
[29] Yan X L, Pang J C and Jing Y L 2019 Ultrasonic measurement of stress in SLM 316L stainless steel forming parts manufactured using different scanning strategies *Materials* **12** 2719
[30] Brytan Z 2017 Comparison of vacuum sintered and selective laser melted steel AISI 316L *Arch. Metall. Mater.* **62** 2125–31
[31] Vrancken B, Thijs L, Kruth J P and Van Humbeeck J 2014 Microstructure and mechanical properties of a novel β titanium metallic composite by selective laser melting *Acta Mater.* **68** 150–8
[32] Tan C L, Zhou K S, Ma W Y, Attard B, Zhang P P and Kuang T C 2018 Selective laser melting of high-performance pure tungsten: parameter design, densification behavior and mechanical properties *Sci. Technol. Adv. Mater.* **19** 370–80
[33] Razavykia A, Brusa E, Delprete C and Yavari R 2020 An overview of additive manufacturing technologies—a review to technical synthesis in numerical study of selective laser melting *Materials* **13** 3895
[34] Shinjo J and Panwisawas C 2021 Digital materials design by thermal-fluid science for multi-metal additive manufacturing *Acta Mater.* **210** 116825
[35] Chen Y H, Clark S J, Leung C L A, Sinclair L, Marussi S, Olbinado M P, Boller E, Rack A, Todd I and Lee P D 2020 *In-situ* synchrotron imaging of keyhole mode multi-layer laser powder bed fusion additive manufacturing *Appl. Mater. Today* **20** 100650
[36] Davidzon M I 2012 Newton's law of cooling and its interpretation *Int. J. Heat Mass Transfer* **55** 5397–402
[37] de Macedo H R, da Silva A G P and de Melo D M A 2003 The spreading of cobalt, nickel and iron on tungsten carbide and the first stage of hard metal sintering *Mater. Lett.* **57** 3924–32
[38] Zhao X, Xu S and Liu J 2017 Surface tension of liquid metal: role, mechanism and application *Front. Energy* **11** 535–67
[39] Hengsbach F *et al* 2018 Inline additively manufactured functionally graded multi-materials: microstructural and mechanical characterization of 316L parts with H13 layers *Prog. Addit. Manuf.* **3** 221–31
[40] Paul A 2013 A pseudobinary approach to study interdiffusion and the Kirkendall effect in multicomponent systems *Phil. Mag.* **93** 2297–315
[41] Chen X X, Shen J, Kecskes L J and Wei Q 2020 Tungsten-based heterogeneous multilayer structures via diffusion bonding *Int. J. Refract. Met. Hard Mater.* **92** 105308
[42] Rahman A H M E and Cavalli M N 2012 Diffusion bonding of commercially pure Ni using Cu interlayer *Mater. Charact.* **69** 90–96
[43] Muster W J, Yoon D N and Huppmann W J 1979 Solubility and volume diffusion of nickel in tungsten at 1640 °C *J. Less-Common Met.* **65** 211–6
[44] Reisner M, Oberkofler M, Elgeti S, Balden M, Höschen T, Mayer M and Silva T F 2019 Interdiffusion and phase formation at iron-tungsten interfaces *Nucl. Mater. Energy* **19** 189–94
[45] Mehrer H 2007 Continuum theory of diffusion *Diffusion in Solids: Fundamentals, Methods, Materials, Diffusion-Controlled Processes* ed H Mehrer (Berlin: Springer) pp 27–36
[46] Fang T T, Chen M I and Hsu W D 2020 Insight into understanding the jump frequency of diffusion in solids *AIP Adv.* **10** 065132
[47] Yusuf S M, Choo E and Gao N 2020 Comparison between virgin and recycled 316L SS and $AlSi_{10}Mg$ powders used for laser powder bed fusion additive manufacturing *Metals* **10** 1625
[48] Malizia A, Rossi R and Cacciotti I 2018 Improvement of the shadow tracking setup as a method to measure the velocities values of dark dust in order to reduce the risks of radioactive releases or explosions *Rev. Sci. Instrum.* **89** 083306
[49] Giannattasio A, Yao Z, Tarleton E and Roberts S G 2010 Brittle–ductile transitions in polycrystalline tungsten *Phil. Mag.* **90** 3947–59
[50] Van Uffelen P and Suzuki M 2012 Oxide fuel performance modeling and simulations *Comp. Nucl. Mater.* **3** 535–77
[51] Gietzelt T, Toth V and Huell A 2016 Diffusion bonding: influence of process parameters and material microstructure *Joining Technologies* ed M Ishak (London: IntechOpen) pp 196–212
[52] Zhang Y W, Li S J, Hao Y L and Yang R 2010 Nanoindentation study on Ti-24Nb-4Zr-8Sn single crystals *Chin. J. Nonferrous Met.* **20** 528–32
[53] Cobbinah P V, Nzeukou R A, Onawale O T and Matizamhuka W R 2021 Laser powder bed fusion of potential superalloys: a review *Metals* **11** 58
[54] Jung B B, Lee H K and Park H C 2013 Effect of grain size on the indentation hardness for polycrystalline materials by the modified strain gradient theory *Int. J. Solids Struct.* **50** 2719–24
[55] Ward L, Junge F, Lampka A, Dobbertin M, Mewes C and Wienecke M 2014 The effect of bias voltage and gas pressure on the structure, adhesion and wear behavior of diamond like carbon (DLC) coatings with Si interlayers *Coatings* **4** 214–30
[56] Huang H, Wu Y Q, Wang S L, He Y H, Zou J, Huang B Y and Liu C T 2009 Mechanical properties of single crystal tungsten microwhiskers characterized by nanoindentation *Mater. Sci. Eng.* A **523** 193–8
[57] Bayat M, Thanki A, Mohanty S, Witvrouw A, Yang S F, Thorborg J, Tiedje N S and Hattel J H 2019 Keyhole-induced porosities in laser-based

powder bed fusion (L-PBF) of Ti_6Al_4V: high-fidelity modelling and experimental validation *Addit. Manuf.* **30** 100835

[58] Yao L M, Huang S, Ramamurty U and Xiao Z M 2021 On the formation of 'Fish-scale' morphology with curved grain interfacial microstructures during selective laser melting of dissimilar alloys *Acta Mater.* **220** 117331

[59] Radovic Z, Jaukovic N, Lalovic M and Tadic N 2008 Positive segregation as a function of buoyancy force during steel ingot solidification *Sci. Technol. Adv. Mater.* **9** 045003

[60] Marcus Y 2017 On the compressibility of liquid metals *J. Chem. Thermodyn.* **109** 11–15

[61] Jain S C and Willander S 2003 Strain, growth, and TED in SiGeC layers *Silicon-germanium Strained Layers and Heterostructures* ed S C Jain and S Willander (New York: Academic) pp 61–90

[62] Yu H-C, Van der Ven A and Thornton K 2008 Theory of grain boundary diffusion induced by the Kirkendall effect *Appl. Phys. Lett.* **93** 091908

[63] Jaseliunaite J and Galdikas A 2020 Kinetic modeling of grain boundary diffusion: the influence of grain size and surface processes *Materials* **13** 1051

[64] Yin J, Zhang W Q, Ke L D, Wei H L, Wang D Z, Yang L L, Zhu H H, Dong P, Wang G Q and Zeng X Y 2021 Vaporization of alloying elements and explosion behavior during laser powder bed fusion of Cu–10Zn alloy *Int. J. Mach. Tools Manuf.* **161** 103686

[65] Zhang W Q, Zhang B P, Xiao H F, Yang H Q, Wang Y and Zhu H H 2021 A layer-dependent analytical model for printability assessment of additive manufacturing copper/steel multi-material components by directed energy deposition *Micromachines* **12** 1394